HTML ABSTRACT + LINKS

Structural and microstructural characterization of nanocrystalline silicon thin films obtained by radio-frequency magnetron sputtering

M. Morales,[a] Y. Leconte, and R. Rizk
Laboratoire Structure des Interfaces et Fonctionnalités des Couches Minces (SIFCOM)-Ensicaen, 6 Bd. du Maréchal Juin, F-14050 Caen, France

Daniel Chateigner
Laboratoire de Cristallographie et Sciences des Matériaux (CRISMAT-Ensicaen, 6 Bd. du Maréchal Juin, F-14050 Caen, France

(Received 22 March 2004; accepted 3 November 2004; published online 14 January 2005)

Textured silicon thin films are deposited by reactive magnetron sputtering in hydrogen-rich plasma on (100)-Si and amorphous SiO_2 substrates. We quantitatively determine, combining x-ray texture analysis, x-ray reflectivity, transmission electron microscopy, atomic force microscopy measurements, and Raman and Fourier transform infrared spectroscopy analyses, the structure (cell parameter and mean electron density) and microstructure (crystalline fraction, preferred orientations, anisotropic crystallite sizes, thicknesses, etc.) of these films. For both kinds of substrates, no perfect $\langle 111 \rangle$ orientation is observed whereas a systematic elongation of the anisotropic Si crystallites along one [111] direction is present. A small elongation of the Si cell parameter of the nanocrystals is found without internal stress. With the substrate to target distance, the crystalline fraction and mean electron density show an opposite behavior to that of the film porosity. The former increases and the latter decreases, and are correlated to the texture evolution. Preferred orientations are observed with texture strengths around two to three times a random distribution, with a tendency to achieve lower strengths for films grown on SiO_2 substrates. The texture components are evolving with the substrate to target distance, with $\langle 110 \rangle$ and $\langle hh\ell \rangle$ (ℓ larger than 2) orientations favored for smaller and larger distances, respectively. All these microstructural properties are correlated with their optical properties and more particularly to their refractive index and their optical band gap. © *2004 American Institute of Physics*. [DOI: 10.1063/1.1841461]

I. INTRODUCTION

Nanocrystalline silicon thin films are promising structures for a wide range of applications in micro- and optoelectronics (flat panel display applications, solar cells, thin-film transistors, etc.).[1] Many studies have been carried out on films produced by vapor phase deposition techniques at moderate to relatively high temperature (600–750 °C), resulting in polycrystalline Si films with columnar growths. Such films exhibit texture components which vary with the deposition conditions and result in residual stresses, and are generally linked to the crystallite morphologies.[2] The lowering of the process temperature, to enable the use of low cost substrates such as common glasses and flexible polymers, is the main challenge to these large areas of microelectronic applications. The use of low temperatures leads generally to the growth of amorphous silicon films, but recently crystallized silicon layers have been achieved by synchrotron-radiation decomposition of disilane,[3] by plasma-enhanced chemical-vapor deposition[4] (PECVD), and also by our group using the reactive magnetron sputtering (RMS).[5] The interactions between the growing surface and the reactive hydride radicals present in the hydrogen-rich plasma originate films by PECVD and RMS techniques that are a mixture of amorphous and crystalline silicon. The growth and crystallization mechanisms are still a matter of debate,[6,7] even though the key role of the highly reactive hydride species is now described by about three models.[8,9] Unfortunately, these mechanisms influence the resulting refractive indices via the crystallite sizes and crystalline phase amounts of the films (in general, layers with large grain size have a small refractive index). Although the growth mechanisms involved are of prime importance, key answers could be provided by a careful characterization of the films, in terms of structure and microstructure. Unfortunately, such a full investigation remains a hard task, for many reasons: (i) the films are composed of polycrystals exhibiting preferred orientations; (ii) the nanocrystals exhibit anisotropic shapes; (iii) they are mixed with amorphous silicon and porosity; and (iv) the films are deposited on various substrates.

We present in this work the results obtained using a recently developed x-ray technique, which is able to combine quantitatively the texture, structure, and anisotropic shape determinations. We complement the x-ray diffraction studies by x-ray reflectivity, Raman and infrared spectroscopies, and electron and atomic force microscopies in order to give access to other microstructural parameters such as porosity, crystalline fraction, etc. In this paper, all the structural and microstructural parameters of the films are correlated to their optical properties (refractive index and Tauc optical gap).

[a]Author to whom correspondence should be addressed; electronic mail: magali.morales@ensicaen.fr

 © 2004 American Institute of Physics

Downloaded 17 Jan 2005 to 192.93.101.134. Redistribution subject to AIP license or copyright, see http://jap.aip.org/jap/copyright.jsp

II. SAMPLES AND EXPERIMENTAL DETAILS

Silicon thin films were grown by a radio-frequency magnetron sputtering technique in a plasma mixture of H_2 and Ar at 200 °C on amorphous SiO_2 (a-SiO_2) and single-crystal (100)-Si substrates. The process used is detailed elsewhere[10] and the deposition conditions were the following: a power density of 2 W/cm^2, a total pressure of 10^{-1} Torr, and an 80% of hydrogen partial pressure. For both kinds of substrates we varied the target-substrate distance d. For a-SiO_2 substrates the d values were 4, 6, 7, 8, 10, and 12 cm corresponding to samples labeled A, B, C, D, E, and F, respectively, while on (100) Si two typical d values were chosen, $d=6$ and 12 cm (samples B' and F', respectively), aiming at a comparison of the substrate effect.

The structural and microstructural characteristics of the films were carefully characterized by the following techniques: conventional x-ray diffraction (XRD), quantitative x-ray texture analysis (QTA), specular x-ray reflectivity (XRR), Raman spectroscopy (RS), transmission electron microscopy (TEM), Fourier transform infrared (FTIR) spectroscopy, and atomic force microscopy (AFM).

For usual XRD and XRR experiments we used a Philips X-Pert MRD at the average Cu $K\alpha$ radiation ($\lambda_{Cu}=1.5418$ Å) equipped with a point scintillator detector. For the former, we measured the films with a step of 0.01° in a symmetric (θ–2θ) mode and then in an asymmetric mode using an incidence angle of $\omega=0.5°$, while the latter scans were restricted to a maximum of 1° in θ range due to the rapid decrease of the signal in our films. To refine the XRR data, we used the REFLEX[11] program using the Fresnel formalism and sample and beam size corrections with a q_z resolution of 0.0006 $Å^{-1}$. An off-specular reflectivity scan was performed in order to check that no any significant diffusion signal was present in the specular scan.

The conventional TEM observations were done on a Jeol 200 CX while the high-resolution TEM images were obtained on a Topcon 002B instrument with a 0.18-nm resolution using cross-sectional specimens. The TEM specimens were prepared using the standard ion-milling technique.

The crystalline volumes (f_c) of the films deposited on a-SiO_2 were estimated by the deconvolution of Raman-scattering spectra as described in details elsewhere.[12] The argon laser beam used ($\lambda=514.5$ nm) had an estimated penetration depth in the silicon of 300 nm. In this approach the polycrystalline asymmetry of the Raman modes and the scattering yield of the amorphous and crystalline species are taken into account.

The FTIR experiments were done using a Nicolet Nexus FTIR spectrometer on thin films deposited on [100]-Si substrates in the 500–4000-cm^{-1} range with a resolution of 2 cm^{-1}. An incident angle of 65° was chosen, near the Brewster angle of the air/silicon interface, in order to reduce intensity losses. All the spectra have been normalized by the film thicknesses and the signal of the [100]-Si substrate has been subtracted.

The surface morphology of the film was studied by AFM on a Nanoscope III extended multimode instrument from Digital Instrument using a tapping mode. We scanned over 10 μm^2 in surface within a 0.2-nm resolution.

In order to correlate the structure and microstructure with the optical properties of the films deposited on a-SiO_2 substrates, we have determined the refractive index of the films by optical transmission spectroscopy using a Perkin–Elmer Lambda 9 ultraviolet-visible spectroscopy (UV-VIS) spectrometer from 0.4 to 4.1 eV. Using the transmission and absorption, $\alpha(\lambda)$, coefficients of the thin films, we have deduced the values of the Tauc optical gap E_g.[13]

As the usual XRD patterns of the films exhibited preferred orientations and anisotropic line broadening, QTA was performed with a simultaneous Rietveld refinement including anisotropic line broadening and film thickness analyses. We used a Huber four-circle diffractometer and a curved position sensitive detector (INEL CPS 120), which spans a 120° range in 2θ, allowing the simultaneous recording of several pole figures and the full diffraction diagram.[14] These latter were measured by scanning the tilt angle of the goniometer, χ, in the range of 0°–35° using 5° steps. We then acquired (for $\chi=35°$) diagrams for the azimuthal angle, φ, in the range of 0°–360° using 5° steps, in order to check for possible in-plane orientation. No significant diagram variation was observed during this latter scan, showing that the sample exhibits a fiber texture. We used an incident angle for the x-ray beam $\omega=14.2°$ corresponding to the Bragg angle of the 111 reflection of the cubic silicon.

For the quantitative analysis of these x-ray diffractograms, we used the material analysis using diffraction (MAUD) program[15] that combines the WIMV method,[16] used to solve the orientation distribution function (ODF), with a Rietveld analysis to extract the microstructural and structural parameters. The integrated intensities, extracted by the Le Bail method, are processed and corrected for the absorption, volume variations, and delocalization effects.[17] The instrumental resolution function has been determined by a full mapping (in ω, χ, and 2θ ranges) of our diffractometer space using the NIST LaB_6 powder standard[18] used for the International Crystallographic round-robin. By the deconvolution of the instrumental broadening from the experimental profile in the Fourier space, using the Lorentzian and Gaussian parts[19] of the profile, the crystallite size and microstrains of the sample are calculated, respectively. The ($hk\ell$) dependence of diffraction line broadening is determined in the program by the use of the Popa rules based on the symmetrized spherical harmonics that allow the modeling of the mean crystallite shape.[20] The thin-film thicknesses are additional parameters fitted during the Rietveld refinement, implemented in the MAUD package via the necessary intensity corrections.[21] These thicknesses have been compared to those measured by profilometry, with a resolution of 10 nm, using a Dektak3 ST instrument. In the MAUD program, the errors on the refined parameters such as cell parameter, anisotropic sizes, and thicknesses, have been estimated as one estimated standard deviation given by the least-square fit. This corresponds to about 67% of the crystallites population for a normal distribution law for the size distribution.

The QTA provides pole figures, which are normalized, in order to be independent of porosity, crystal state, stresses,

Downloaded 17 Jan 2005 to 192.93.101.134. Redistribution subject to AIP license or copyright, see http://jap.aip.org/jap/copyright.jsp

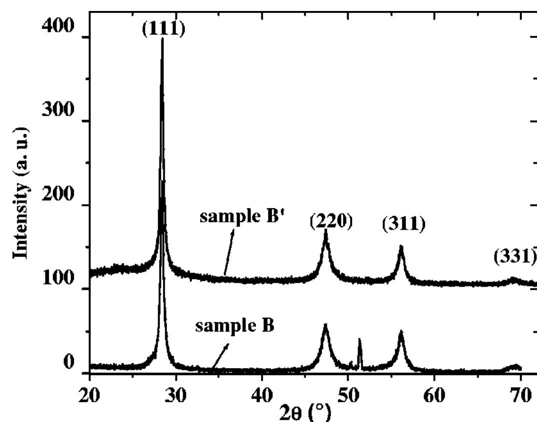

FIG. 1. Asymmetric XRD patterns measured at $\omega=0.5°$ for samples B and B' deposited, respectively, on (100)-Si and a-SiO_2 substrates. Note, for example, for sample B' the strong anisotropic line broadening as attested by the full width at half maximum values of 0.39° and 1.13°, respectively, for the (111) and (220) reflections. The narrow peak at 51.5° is the $\lambda_{Cu}/2$ contribution of the Si single-crystal substrate (400) planes and illustrates the instrumental broadening around (220).

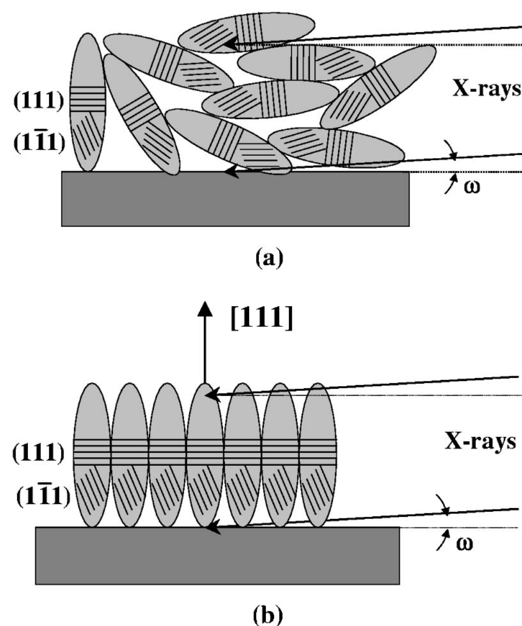

FIG. 2. Schematics of anisotropic crystallites having (a) a random orientation and (b) a texture with one [111] direction perpendicular to the film plane.

and thicknesses from film to film. This normalization is operated through the calculation of distribution densities that are expressed as multiples of a random distribution (mrd). The ODF allows then the recalculation of the experimental pole figures for comparison with the observed data and first reliability evaluation. The statistical ODF reliability is evaluated by the calculation of the RP_0 factors[22] while the overall texture strength is estimated by F^2, the texture index value.[23] Since we determined that our film textures are axially symmetric around the normal to the film plane (fiber textures), the inverse pole figure calculated for this normal direction 001 is a complete representation of the ODF. We then chose to illustrate the exhibited textures using such inverse pole figures. Data reduction and calculations of the inverse pole figures were done using the GOMAN, POFINT,[24] and BEARTEX[25] packages, respectively.

III. RESULTS AND DISCUSSION

A. XRD results

1. X-ray diffraction pattern from single sample orientation

To gain some insight on the crystallization degree of our films we compare in Fig. 1 two typical XRD patterns recorded on samples B and B' deposited on two different substrates. The measurement carried out at a fixed low incident angle of 0.5° allowed to magnify the irradiated volume and avoided the long acquisition time necessary in the Bragg–Brentano geometry. The background observed for sample B is smoother than the one of sample B'. This latter exhibits diffuse scattering for angles lower than 30°, revealing the contribution of an amorphous part in the whole x-ray signal. Consequently, at first sight, the crystalline fraction of the film deposited on (100)-Si (sample B) appears higher than its counterpart for sample B' grown on a-SiO_2. However, the spectrum of this latter would include the contribution part of the amorphous substrate, preventing any quantitative estimate of the crystalline fraction which would be determined more appropriately further by RS. The diagram measured on sample B shows a narrow peak coming from the single-crystal substrate around $2\theta=51.5°$, which corresponds to the $\lambda_{Cu}/2$ contribution of the (400) planes. Compared to this latter peak, one can see that both patterns show strong line broadening for the silicon nanocrystal film. Also, preferred orientations of the crystallites are observed (the peak intensities are not the ones of a randomly oriented powder). The mean crystallite shape has been estimated in the first step from a Debye–Scherrer analysis of the θ–2θ scans and taking into account in this formula the instrumental broadening correction in the same angular range.[26] We recall that the Debye–Scherrer formula is valid only in the symmetrical mode and assumes an isotropic shape of the coherent domains. With our experimental configuration, the upper and lower limits for size determination with this formula done by the step of our measurements (0.01°) and by the choice of the considered angular range around every $hk\ell$ reflection (5°) are, respectively, 820 and 1.6 nm. The mean crystallites shape is found to be an ellipsoid with an elongation along the [111] direction, reaching a relatively large value of around 29 nm compared to the expected grain size.

However, in our case from a single measurement as the one shown in Fig. 1, the mean crystallite sizes determination is affected by peculiar artifacts. As a crystallographic texture is present, for one measured orientation of the sample, only some $\{hk\ell\}$ planes are preferentially brought to diffraction, while the others are not detected. Consequently, crystallite sizes may be severely biased since they are only estimated from these diffracting planes. Figure 2 illustrates these aspects for a sample exhibiting anisotropic crystallite shapes with ellipsoids elongated along the [111] direction. In the case of crystallites randomly oriented in the sample [Fig. 2(a)], the mean crystallite size as deduced from the 111 line is an average over the 111 multiplicity. Since for a single

Downloaded 17 Jan 2005 to 192.93.101.134. Redistribution subject to AIP license or copyright, see http://jap.aip.org/jap/copyright.jsp

crystal of Si, the (111) plane is at 70.53° from $(1\bar{1}1)$, $(11\bar{1})$, and $(\bar{1}11)$, the mean size along ⟨111⟩ will take a value between the short and long axes of the ellipsoid. This approach remains valid for any $hk\ell$ diffraction line, resulting in a systematic lowering of the shape anisotropy when calculated from a single diagram. For the case of a textured sample having (111) planes mostly parallel to the sample surface and [111] elongated crystallites perpendicular to it [see Fig. 2(b)], the long dimension of the crystallites is more favored than the short one, which has to be probed with other $hk\ell$ lines. However, the long dimension is still underestimated if low ω values are used, because this configuration does not ensure to probe the maximum of the distribution of the crystallites orientation. Such biased estimations are often encountered in works reporting silicon crystallite size determination using the Scherrer formalism, resulting in overestimated sizes with underestimate of shape anisotropy.[27–30] We prefer this approach to the integral width approach,[31] which Houben *et al.*[32] used, or even better the direct Fourier deconvolution of the signal from the x-ray profile[17] used in this work.

The cell parameter of the silicon structure may also be biased when determined from single pattern measurements. If structural strains are imposed by the substrate or the small crystal sizes, these ones will differ among differently oriented $(hk\ell)$ planes, resulting in peak shifts not corresponding to the mean shifts over all the orientations. In turn, a quantitative texture analysis will be difficult to perform without the exact determination of the crystal structure.

2. Combined x-ray diffraction analysis

To overcome the aforementioned problems, we performed measurements of the full diffraction diagrams for multiple orientations of the sample. This allows one to obtain a better estimate of the anisotropic shapes and cell parameter, weighted by the volumic ratio of material in a given orientation. This is achieved by the simultaneous analysis of the anisotropic shape and the quantitative textures through the so-called "combined refinement."[33,34] Furthermore, the procedure enables to refine the film thickness (as probed by x rays).[19] A typical full texture analysis involves the measurements of a large number of diagrams, typically of the order of 1000 for a grid resolution of 5° used here (for as many sample orientation). However, due to the high crystal symmetry of Si, we only require χ scans up to 35°, and taking into account that the texture is of fiber type only χ scans can be used. This lowers the number of diagrams to be measured to eight corresponding to the χ sample orientations. With such measurements, for a cubic unit cell, we calculated using the MIMA approach of BEARTEX[23] that a minimum value of four intersections of pole figure projection paths is obtained for all orientation cells (Fig. 3). This ensures a satisfactory determination of the ODF.[35] Consequently, the texture reliability factors RP_0 (Ref. 20) as reported in Table I are generally around 1% and never exceed 3% hence attesting the good ODF definition. This reliability is also demonstrated by the comparison of experimental and simulated diffraction diagrams using the combined analysis (Fig. 4) with reliability factors R_B, R_w, and R_{exp} around 5%.[36] Such reliabilities,

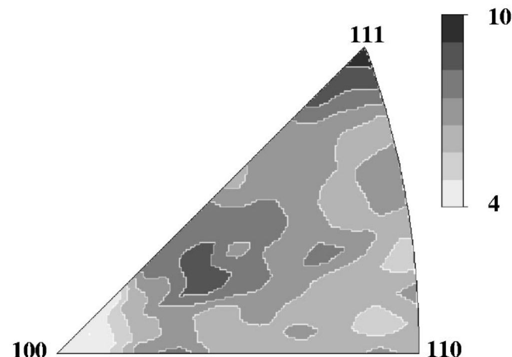

FIG. 3. Plot in cubic crystal reference frame with the evaluation of the orientation space coverage for the analyzed radial distributions. The levels are the numbers of observations per ODF cell. Notice that all the cells are determined by at least four observations whereas a minimum requirement of three is mandatory. Linear scale and equal area projection.

if they could be achieved by simple texture parameter fits such as those used in the March–Dollase[37] or Lotgering[38] approaches, would not correspond to a physically understandable model of the texture in our case, because of the fairly complex ODF of our samples, as will be seen in the next sections.

3. Stress-free crystal structure

Whatever the deposition conditions and the substrate considered (Table I), the film structure was found to be consistent with a regular diamond cubic structure of Si with a cell parameter a around 5.44 Å. The observed values are always larger than those for bulk silicon and correspond to a mean lattice expansion of $\Delta a/a = 0.07\%–0.28\%$. However, no peak shift was observed when tilting the samples in χ, which indicates that the measured cell parameters correspond to the stress-free state of the silicon nanoparticles. This implies a thermodynamic origin of the larger cell parameters compared to the bulk, the surface energy taking a progressively larger influence as the crystallite size decreases. Such cell parameters are indeed larger than that reported in the literature for microcrystalline silicon films for similar film thicknesses.[39] However, the anisotropic expansion of the cell parameters reported in Ref. 39 when tilting the sample is interpreted as a tetragonalization of the unit cell. Such a unit-cell distortion is much more probably due in our opinion, to the effect of residual stresses stabilized in their films, and which are absent in our films (we did not observe any peak shift when tilting the samples). Faivre and Bellet[40] observed also a lower lattice expansion on porous silicon (PS) layers obtained by electrochemical etching of single-crystal silicon. In this case, the PS layer is nearly single crystalline and still under single-crystal stress, giving less deformation of the layer, while in our case the crystal size effect predominates on porosity effects.

4. Crystallographic texture

For a given substrate, if the overall texture strength of the films appears almost constant, the XRD characterizations show that the texture components are evolving as the d distances increase. Figure 5 illustrates this evolution of 2θ dia-

Downloaded 17 Jan 2005 to 192.93.101.134. Redistribution subject to AIP license or copyright, see http://jap.aip.org/jap/copyright.jsp

TABLE I. List of structural and microstructural parameters of the films resulting from the refinement and associated reliability factors R (R_w: weighted, R_B: Bragg, R_{exp}: experimental, and RP_0: ODF factor for all distribution densities). The texture index is F^2. Numbers in parentheses represent errors on the last digit as estimated by one standard deviation. The thicknesses measured by profilometry are with a resolution of 10 nm.

					Anisotropic sizes (Å)			Texture parameters			Reliability factors (%)			
Sample	d (cm)	a (Å)	Measured thickness (nm)	RX thickness (nm)	[111]	[220]	[311]	Maximum (mrd)	Minimum (mrd)	F^2 (mrd^2)	RP_0	R_w	R_B	R_{exp}
A	4	5.4466 (3)	700	⋯	94 (3)	20 (1)	27 (1)	1.95	0.4	1.12	1.72	4.0	3.7	3.5
B	6	5.4439 (2)	1350	711 (50)	101 (3)	20 (1)	22 (1)	1.39	0.79	1.01	0.71	4.9	4.3	4.2
C	7	5.4346 (4)	1530	519 (60)	99 (3)	40 (1)	52 (2)	1.72	0.66	1.05	0.78	4.3	4.0	3.9
D	8	5.4461 (2)	1465	1447 (66)	100 (3)	22 (1)	33 (1)	1.57	0.63	1.04	0.90	5.5	4.6	4.5
E	10	5.4462 (2)	1470	1360 (80)	98 (3)	20 (1)	25 (1)	1.22	0.82	1.01	0.56	5.0	3.9	4.0
F	12	5.4452 (3)	1208	1110 (57)	85 (2)	22 (1)	26 (1)	1.59	0.45	1.05	1.08	4.2	3.5	3.7
B’	6	5.4387 (3)	1350	1307 (50)	89 (3)	22 (1)	28 (1)	1.84	0.71	1.01	1.57	5.2	4.7	4.2
F’	12	5.4434 (2)	1200	1214 (18)	88 (3)	22 (1)	24 (1)	2.77	0.50	1.12	2.97	5.0	4.5	4.3

grams recorded at $\omega = 14.2°$ and $\chi = 0$, for two films deposited on a-SiO_2 at interelectrode distances $d = 10$ cm and $d = 4$ cm. While a strong 111 peak is observed for $d = 10$ cm (sample E), this peak is strongly reduced at $d = 4$ cm (sample A). All the examined films are exhibiting fiber textures with multiple fiber components.[20] Figure 6 illustrates this multiple component fiber texture for sample E, using the five radial density profiles of the main pole figures recalculated from the ODF refined by the combined analysis on our XRD spectra. Two main components of orientation are observed with ⟨111⟩ and ⟨400⟩ directions aligned close to the film E normal (from $\chi = 0° - 10°$), as denoted by the density reinforcement of these two corresponding profiles [Figs. 6(a) and 6(b)]. However, other fiber components may exist in this film, which would not be detected using only these five radial distributions, because the available 2θ range of our instrument would not provide more measurable distributions in this system. The other potential components are included in all the measured profiles but are not easily seen from them since they are located at high χ values and are overlapped with others. A full representation of all fiber components is seen in inverse pole figures (Fig. 7). As evidenced on this figure, films deposited on a-SiO_2 substrates show a large texture dependence with the interelectrode distance. Although the overall texture strength of the films appears almost unaffected by the d variation [with F^2 values around 1.2 mrd^2 at maximum and 001 inverse pole figure maxima not larger than 2 mrd (Table I)], the resulting texture components are strongly influenced. The closest distance (sample A) favors an orientation with ⟨110⟩ directions aligned with the films normal as a major texture component (Fig. 7) whereas minor components are also observed with ⟨100⟩ and ⟨124⟩ directions of crystallites along the normal. The ⟨110⟩ orientation is destabilized for distances larger than 4 cm and is no longer present for $d = 6$ cm (sample B). This ⟨110⟩ component removal is accompanied by a slight tilt of the ⟨100⟩ (which could correspond to a $\langle h0\ell \rangle$ alignment with ℓ around 11) and the appearance of a large component centered on ⟨221⟩-like orientation. Since this component is largely dis-

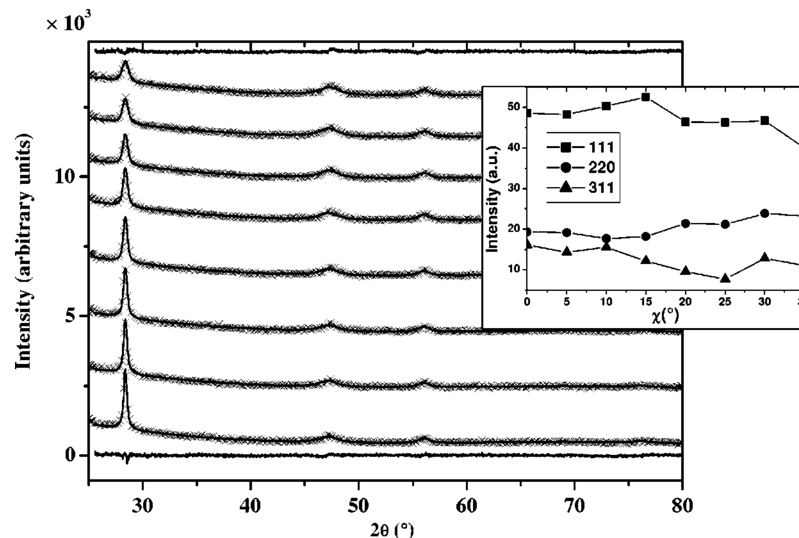

FIG. 4. Typical XRD diagram measured (crosses) on sample D ($d = 8$ cm) at different χ positions ($\chi = 0°$ at bottom and $\chi = 35°$ at top) showing the broad and anisotropic-diffracted lines and the corresponding simulated spectra (solid line). The bottom and top diagrams correspond to the difference diagram (observed calculated) for, respectively, $\chi = 0°$ and 35°. Inset shows the texture presence by the χ scans of the three main integrated intensities (background is subtracted). Note the particularly high 311 intensity and the nonconstant variations of the lines with χ. The diagrams have been shifted vertically for a better understanding.

Downloaded 17 Jan 2005 to 192.93.101.134. Redistribution subject to AIP license or copyright, see http://jap.aip.org/jap/copyright.jsp

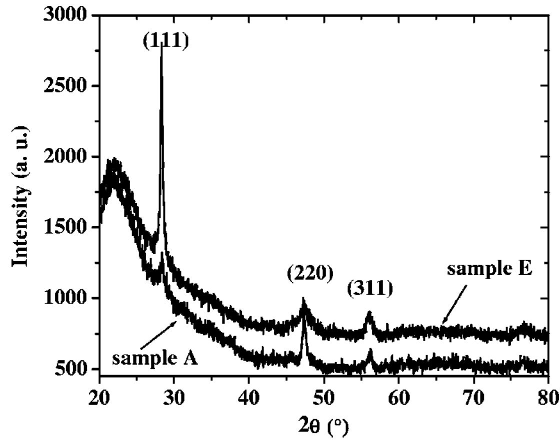

FIG. 5. Asymmetric XRD scans obtained with an incident angle $\omega = 14.2°$, corresponding to the Bragg angle of the (111) reflection, for $\chi = 0°$. Note the strong decrease of the 111 line for sample A ($d = 4$ cm) compared to sample E ($d = 10$ cm).

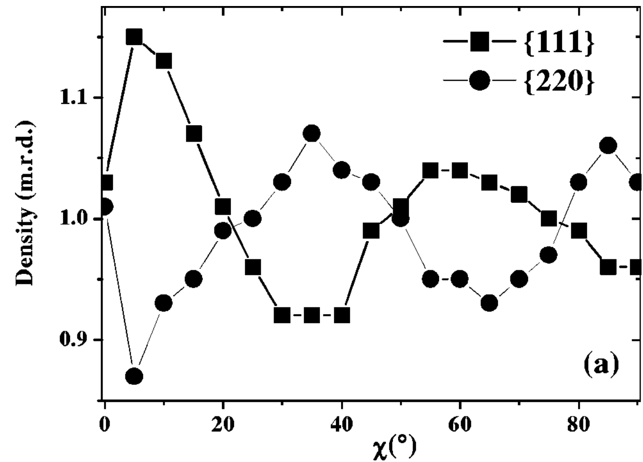

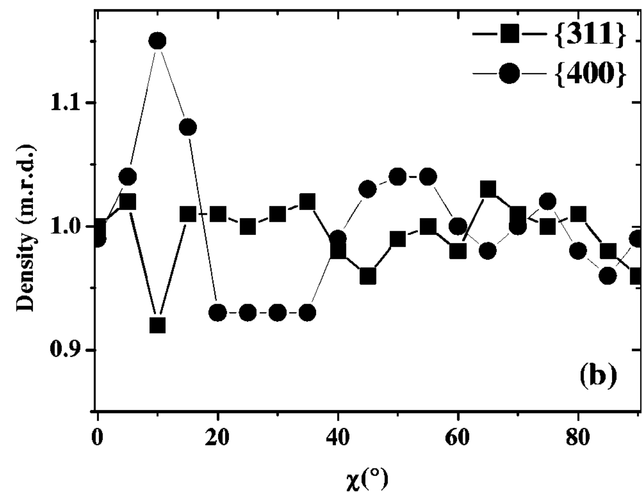

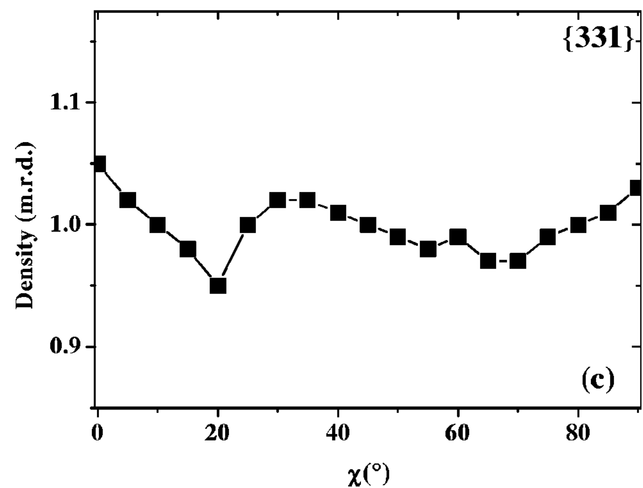

FIG. 6. Characteristic radial density profiles of the main pole figures recalculated from the ODF and refined in the combined analysis using the MAUD program for sample E: (a) {111} and {200}, (b) {311} and {400}, and (c) {331} distributions.

tributed, it corresponds to a set of closely oriented directions such as ⟨332⟩, ⟨443⟩, ⟨554⟩, …, that can be present in this film, too. An interesting behavior is the progressive shift of this latter component towards a ⟨111⟩ orientation for increasing d (samples B–F, see Fig. 7 at the bottom for checking indices). Comparing films B and E, one clearly sees the general trend starting in B from orientations around ⟨221⟩ and reaching ⟨443⟩ or ⟨553⟩ in E. However, if the texture component would tend to coincide with a ⟨111⟩ orientation for largest d's (that is along the largest dimension of the crystallites), no pure ⟨111⟩ orientation is observed that would correspond to a favored growth at the bulk state in the diamond structures.[41] Furthermore, for the largest distance (sample F) a ⟨112⟩ orientation starts to appear. The ⟨100⟩-inclined orientation is fully removed for intermediate distances (samples C and D), then reappears for larger distances up to 12 cm.

Using (100)-Si single crystals as substrates strongly stabilizes the ⟨100⟩ orientation (Fig. 7). Since in our elaboration conditions hydrogen species etch the native Si oxide layer of the substrate, this orientation may correspond to a heteroepitaxial component with [100] directions of the film aligned with the ones of the substrate. However, no heteroepitaxial but fiber texture is observed, implying that, if heteroepitaxy takes place at the interface with the substrate, it is rapidly removed through the thickness of the film. This would originate from island growing directly on the bare (100)-Si substrate, which stack into fiber textures along the [100] direction, a process helped by combining small crystals having large unit-cell parameters with partial crystallization of the films. This fiber texture preludes the columnar structure evidenced in Sec. III B by TEM and which is favored by the crystallization mechanism induced by the SiH_2 species identified by FTIR as reported and discussed further (Sec. III C).

The minimum values of the ODF (Table I) are relatively high, from 0.4 to 0.82 mrd, indicating that 40%–82% of the volume of the material is randomly oriented (not textured). The texturation of the crystalline part of the film seems to be favored at low and high d values (typically lower than 6 cm and larger than 10 cm) whereas the textured volumic ratio is about 72% in average for $6\ \text{cm} < d < 10$ cm. Comparing films B and F to B' and F', respectively, one can observe that this texturing effect at large distance is favored by the a-SiO_2 substrates, even though it does not correspond to the development of the same texture components. Due to the relatively high random component, any anisotropic property than one could observe on such materials will then be the

Downloaded 17 Jan 2005 to 192.93.101.134. Redistribution subject to AIP license or copyright, see http://jap.aip.org/jap/copyright.jsp

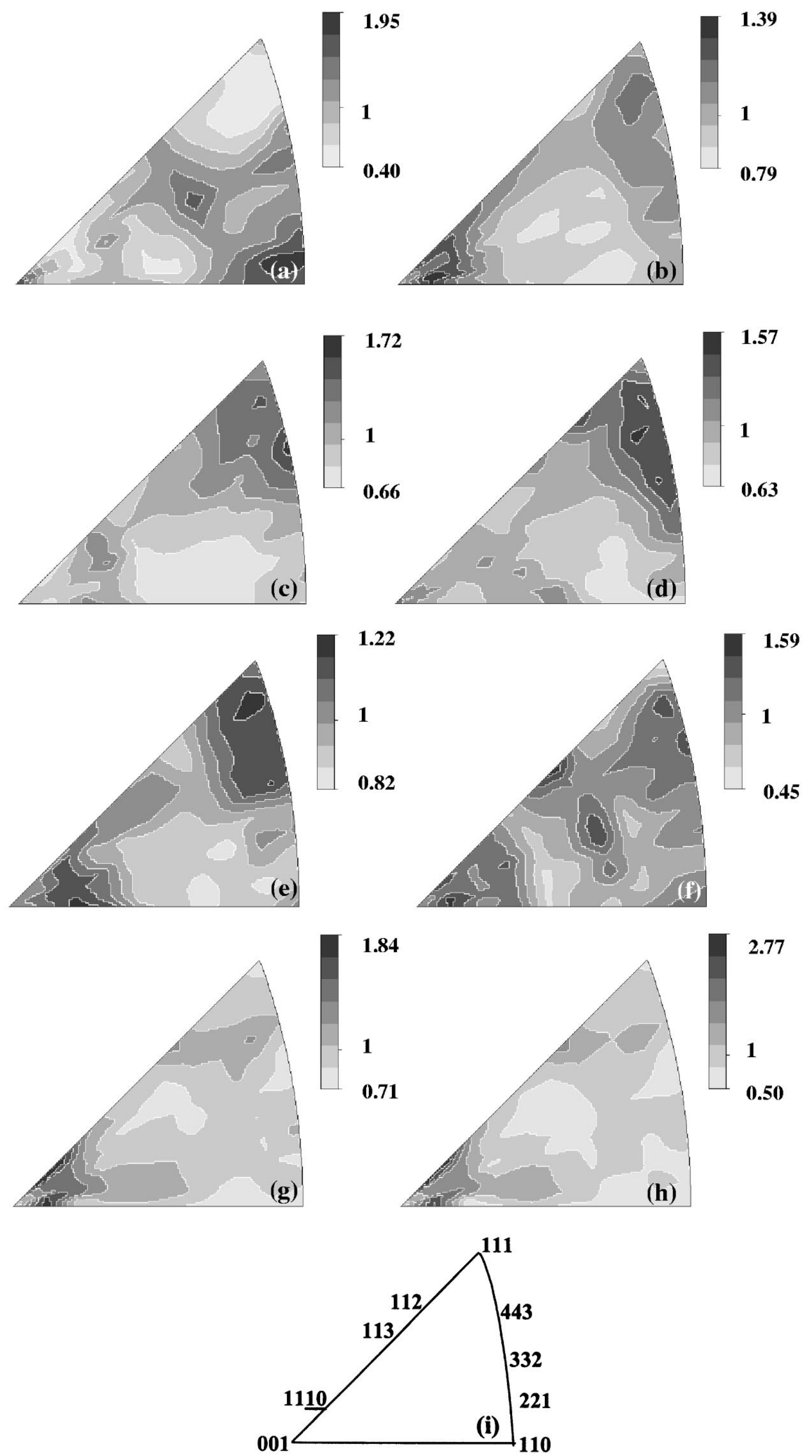

FIG. 7. (a)–(f) 001 inverse pole figures for samples deposited on a-SiO_2 (samples A–F, respectively) and on (100) Si for (g) samples B' and (h) F'; (i) their corresponding pole locations are indicated by their Miller indices in the crystal frame. Equal area projections and linear distribution density scale.

consequence of only 60%–18% of the total volume, hereby considerably decreasing the probability of observation of such anisotropy.

Considering the numerous textural components present in the same film, a texture discussion from the simple diffracted intensity or intensity ratio, as often reported in the literature[28,29,42–44] is a very hazardous task. Authors generally find ⟨110⟩ orientations coming from columnar growth at relatively high temperatures (typically in the range of 600–700 °C), while our low-temperature process only produces this kind of orientation at small interelectrode distances,[45,46] and is interpreted by a fastest growth along ⟨110⟩ directions. However, ⟨110⟩-preferred growth cannot by itself only explain the columnar microstructure since six crystallographically equivalent [110] directions would act, resulting in more isotropic growth shapes. Also, since [111]-elongated crystallites are found in this work whatever the texture, including ⟨110⟩-oriented films, [111] is probably the

Downloaded 17 Jan 2005 to 192.93.101.134. Redistribution subject to AIP license or copyright, see http://jap.aip.org/jap/copyright.jsp

largest growth speed at the conditions used for our films. This is coherent with observations by Yang *et al.*,[47] which revealed mixtures of ⟨111⟩ and ⟨311⟩ orientations at moderate temperatures in polycrystalline silicon. However, a direct comparison with polycrystalline films is not straightforward since our films are containing amorphous silicon in a non-negligible amount. Such an amorphous content can give rise to more homogeneous nucleation and may explain why we do not observe in our nanocrystalline films the same orientation dependency with thickness and temperature as other authors.[45–50] Also, since no stress could be observed, no stress-driven texture development model[48] can be applied.

5. Texture versus cell parameter

Concerning the correlation between the unit cell and the texture components, one can observe that when one of the major texture components (i.e., ⟨100⟩, ⟨110⟩, and the nearly ⟨111⟩ orientation) is stabilized, the cell parameter tends to be larger for both kinds of substrates. For instance, comparing films A and B on a-SiO_2, in which the highest texture component is ⟨110⟩, the unit-cell parameter is 5.4466±0.0003 Å in film A which shows the largest texture strength (highest texture index), whereas the lesser textured film B exhibits a cell parameter a=5.4439±0.0002 Å. The same tendency occurs for films deposited on (100) Si (samples B' and F'), which exhibit both a stronger ⟨100⟩ texture, the largest cell parameter being observed for the highest texture of film F'. In films C and D, the observed highest orientation near ⟨111⟩ is concomitant to the largest cell parameter observed in our films whereas intermediate textures (films C and F) result in smaller unit cells. For similar texture strengths such as those for films A and B', the ⟨100⟩ orientation seems to result in relatively lower cell parameter. Using high-resolution x-ray diffraction, Faivre and Bellet[40] observe a slight anisotropic deformation of the lattice, a less lattice expansion being observed for PS layers elaborated by etching (100) than (111) single-crystal silicon. They observe on individual crystals what we statistically observe via QTA information, but our nanocrystals are much expanded due to their small sizes.

6. Anisotropic mean crystallite sizes

The strong and anisotropic broadening of the diffracted lines observed in Fig. 1 is due to anisotropic shapes of individual crystallites. Thanks to the combined analysis, the mean crystallite shape was refined, corrected for texture effects. Whatever the deposition conditions and the substrate nature, the mean crystallite shape corresponds to an ellipsoid elongated along the [111] direction and almost isotropic in perpendicular directions (Table I). As schematically illustrated in Fig. 8, the average crystallite size along [111] is around 90 Å for sample D (which is around four times less than the value estimated by the Scherrer formula) and 20–40 Å in the perpendicular directions. The crystal shape anisotropy is therefore much larger than the one deduced from single pattern analysis.

In our films, we could not detect any significant Gaussian contribution in any of the peaks (no microstrains are present). This observation means on one hand that the nanocrystals have nicely grown without internal d-spacing dispersion, and on the other hand that no dispersion of d spacing from crystal to crystal exists in a given film.

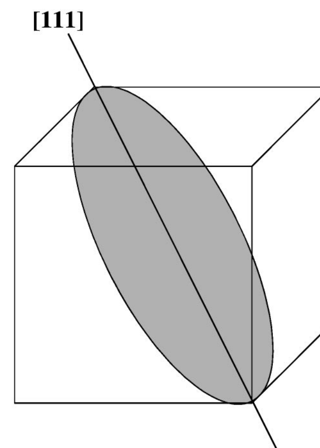

FIG. 8. Schematic mean crystallite shape for sample D represented in a cubic cell, as refined using the Popa approach and exhibiting a strong elongation along [111].

Whatever the substrate nature no pure ⟨111⟩ texture could be observed, but a systematic elongation of the crystallites along this direction. This apparent absence of correlation between orientation and crystal shapes is the consequence of the growth interruption induced by the fabrication process, preventing more regular growth schemes from occuring such as in heteroepitaxial growing. However, looking closer at mean crystal sizes along ⟨111⟩ and ⟨220⟩ directions, one observes that films in which the ⟨100⟩ orientation is present show a smaller crystal shape anisotropy. On (100)-Si substrates exhibiting a strong ⟨100⟩ orientation, but also for film F on a-SiO_2, the ⟨111⟩ mean dimension is around 85 Å, while that along ⟨220⟩ is around 22 Å. Sample A exhibiting a major ⟨110⟩ orientation but still a minor ⟨100⟩ shows ⟨111⟩ mean dimension around 94 Å, at least 5 Å less than films without the ⟨100⟩ component (samples B, C, D, and E). Interestingly, Houben *et al.*[32] found similar crystallite sizes in nontextured and microstrain-free microcrystalline films; but with a reverse relationship of the shape anisotropy. Compared to our results on textured films, this definitely tends to demonstrate a textural relationship on anisotropic crystal shapes.

7. Profilometry and XRD thicknesses

According to profilometry measurements, the thicknesses of all films, except A, are around 1300 nm (Table II). The thicknesses refined by XRD and measured by profilometry are in good agreement for films deposited at larger distances on a-SiO_2 and whatever the distance for films deposited on Si (films D–F'). For these films we observe, however, a systematically slightly smaller thickness by XRD. Thicknesses deduced by XRD for films (A–C) deposited at distances lower than 7 cm on a-SiO_2 are showing large discrepancies with the ones measured by profilometry (approximately half the profilometry value for films B and C). For film A, the thickness is even not determinable by XRD (the refinement procedure diverges).

Downloaded 17 Jan 2005 to 192.93.101.134. Redistribution subject to AIP license or copyright, see http://jap.aip.org/jap/copyright.jsp

TABLE II. List of the refined parameters available using reflectivity analysis for samples B (d=6 cm) and E (d=10 cm) : q_c represents the critical wave vector, β the absorption coefficient, σ_{rms} the roughness, and P the porosity of the two layers used for the refinement. Numbers in parentheses represent errors on the last digit.

Distances d (cm)	Layers	q_c (Å^{-1})	P (%)	σ_{rms} (Å)	$\beta(10^{-7})$	XRR thickness (nm)
10	Covered layer	0.02945(5)	13 (3)	12.9(2)	1.8 (2)	1200 (1)
	Top layer	0.0265 (7)	30 (4)	80 (1)	0.29(2)	16.7(9)
6	Covered layer	0.02724(5)	26 (3)	6.6(5)	1.8 (1)	1210 (2)
	Top layer	0.0245 (1)	40 (5)	69 (1)	0.31(6)	10.8(6)

Since the XRD-related thicknesses are refined from the diffracted intensity[19] (crystalline part of the films), these effects may be assigned to the presence of an amorphous silicon phase or to porosity. Since for the thinnest film (sample A) no XRD value could be obtained, a larger porosity or amorphous phase development is expected at the first growth stages, but none of the two techniques is able to discern between amorphous phase or porosity.

8. X-ray reflectivity

Although our films are too thick to allow the observation of oscillation in our x-ray reflectivity spectra, the critical angle value can provide a measurement of the mean electronic density of the layers. Figures 9(a) and 9(b) show typical specular reflectivity curves recorded for sample E (d =10 cm) and sample B (d=6 cm), respectively. In addition to the absence of oscillation, as expected, the decrease of the curve in scattering wave-vector transfer q_z is very pronounced, indicating a roughness dominated phenomenon. We can observe two regimes in the curves: a first strong decrease after the total reflection regime which extends up to about 0.03 Å^{-1} and a second regime between 0.03 and 0.07 Å^{-1}, before the curves reach asymptotically the background. These two regimes prevent a correct refinement by a single layer model. A thin overlayer with a higher roughness has to be considered in the model in order to reproduce the high surface roughness as introduced, for instance, by Fujiwara *et al.*[51] In such a layer, thickness, absorption, roughness, and the critical scattering wave-vector transfer q_c are strongly correlated and only characterize the average electron density of a strongly rough and porous media. The XRR results for the two films are detailed in Table II. The strong decrease corresponds to a root-mean-square roughness σ_{rms} of 80 Å for the top layer of sample E, as refined by a Fresnel formalism, giving a predominant contribution of the background for q larger than 0.07 Å^{-1}. On the figure we indicate for comparison a $1/q^4$ power-law decrease valid for a perfectly flat surface. The critical scattering wave-vector transfer q_c for the bulk of the film (deep layer) is 0.02945 Å^{-1}, corresponding to a mean electron density of 0.62 e$^-$Å^{-3}. These values are lower than those for bulk silicon[52] (0.0316 Å^{-1} and 0.708 e$^-$Å^{-3}, respectively), which is a clear indication of the porosity of the films. From these analyses, the mean electron density increases with the distance d (in sample B it takes the value of 0.02724 Å^{-1}) for both top and covered layers, leading to a better understanding of the small XRD thickness refined for the thinner films (Table I). Due to a large roughness, the electron density of the material is considerably lower in the top layers as denoted by the difference in q_c values. The roughness of the films is not extended by more than 170 Å in sample E with a mean value of 80 Å.

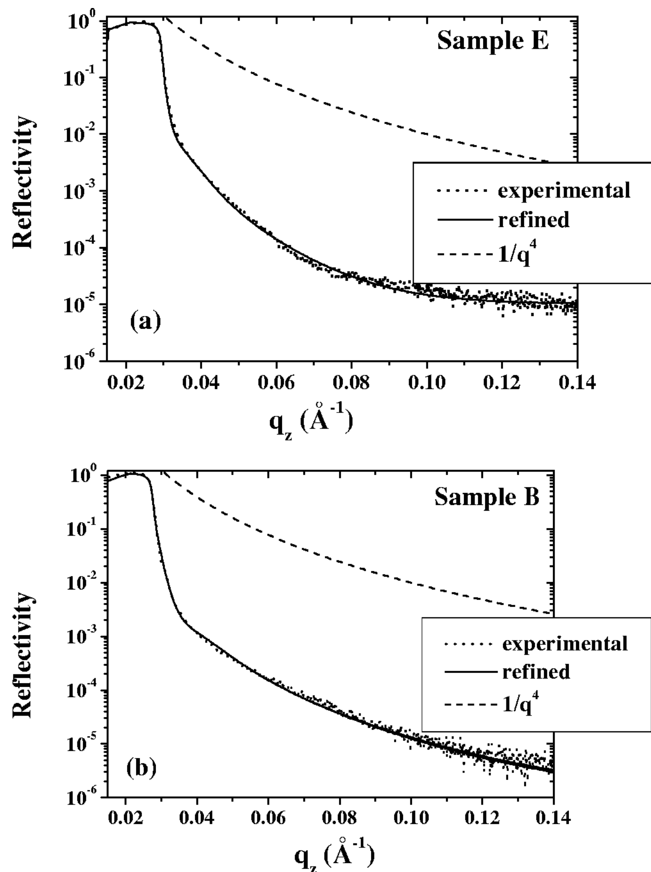

FIG. 9. Experimental and refined x-ray reflectivity curves (a) for sample E (d=10 cm) and (b) sample B (d=6 cm). The $1/q^4$ curve illustrates at large q_z's a sample without roughness.

XRR is a useful investigation method to probe the film porosities (P). Buttard *et al.*[53] proposed an approach using the ratio between the measured critical angle (θ_c) and the theoretical bulk value for silicon ($\theta_{c\ Si}$=0.222°)

$$P = 1 - (\theta_c/\theta_{c\ Si})^2. \quad (1)$$

For large distances (sample E, d=10 cm) in our films we obtain porosities near 13% in the bulk of the material and 30% in the near-surface region, i. e., in a probed layer thickness of about 10 nm. However, such porosity reaches 26% and 40%, respectively, at smaller distances (sample B, d =6 cm). Since our films are composed of mixed amorphous

Downloaded 17 Jan 2005 to 192.93.101.134. Redistribution subject to AIP license or copyright, see http://jap.aip.org/jap/copyright.jsp

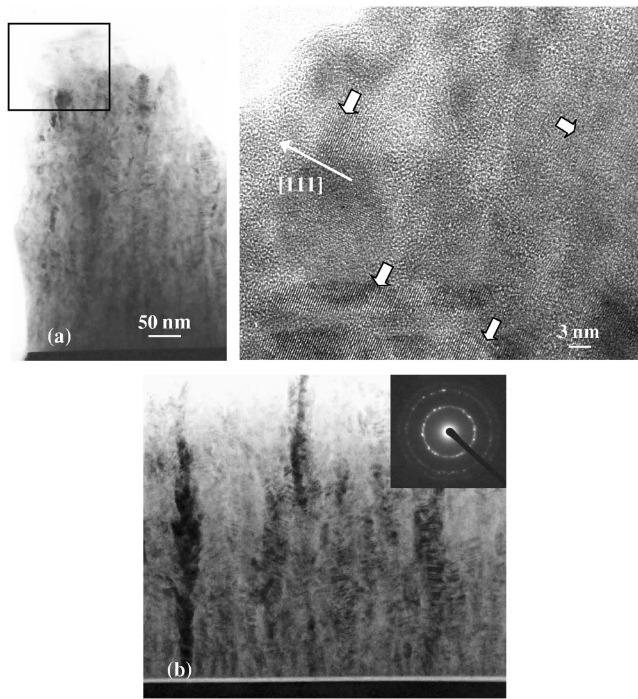

FIG. 10. Typical cross-section TEM images of samples deposited at (a) $d = 6$ cm (sample B) and (b) $d = 12$ cm (sample F), with in inset the corresponding selected area electron diffraction (SAED) pattern. The area limited on (a) by the rectangular frame is magnified on the right side and put in evidence the presence of nanograins (pointed out by white arrows) embedded in an amorphous environment.

and crystalline particles with different mean electron densities, such an approach results in a slightly biased estimation of the real porosity. However, it strongly underlines the porous character of the films.

B. TEM

The discrepancy observed between the XRD and profilometry thicknesses is mainly attributed to the film porosity. Such a porosity is illustrated in Fig. 10 on cross-sectional TEM images of samples B and F for which Raman spectra analyses (reported below) indicate a crystalline ratio of 80% and 68%, respectively. These micrographs exhibit a highly columnar structure of silicon, similar to that observed by Vallat-Sauvain *et al.*[29] and Houben *et al.*,[32] with an average column width lower than 30 nm (sample F), within a highly porous and amorphous environment near the top of the layer[10] [inset of Fig. 10(a)]. In contrast, an almost complete crystallization with a relatively compact tissue is observed in the deep region. These observations provide strong support to the necessary introduction of two layers for the earlier-mentioned refinement of the XRR curves. Contrary to the observations reported in Refs. 29,32, the selected area diffraction diagram [see inset of Fig. 10(b)] does not show any amorphous contribution, but a polycrystalline powderlike pattern with strong reinforcements. These latter indicate the presence of larger crystallites in the probed volume. For the lower distances, the columns are shorter and unconnected along the depth of the film probably due to the accumulation of nanopowders, whereas the column contrast appears more homogeneous for larger d's. This is coherent with the increase of the compactness with d already shown by XRR.

The TEM observations are consistent with those reported by many authors[29,51,54] and also with our XRD analyses, providing coherent domain sizes lower than 10 nm on average. These domains are much smaller than the apparent crystal sizes probed by TEM, and porosity, resulting in small apparent XRD thicknesses. Indeed, there is no *a priori* relationship between coherent domain sizes as determined by diffraction and grains as seen in an image model by TEM. Some authors even report columnar growth of perfectly amorphous silicon.[55] For a direct comparison of XRD and TEM crystallite shapes and sizes, we report a high-resolution TEM image of the near-surface region of the film B in Fig. 10(a). It shows individual single crystallites embedded in a locally amorphous silicon matrix and approximately of the size and shape of XRD mean values. From the figure scale bar one can see the perfectly coherent results obtained by the two techniques.

Contrary to Houben *et al.*[32] no microtwinnings could be observed in our films, as expected, since our films present a columnar growth resulting in fiber textures, i.e., without orientation relationship in the plane of the samples.

C. Crystalline ratio and hydrogen content

RS studies have been carried out in order to determine the crystalline volume fraction f_c. In the particular case of silicon films with a mixed composition of amorphous and nanocrystalline phases, the Raman spectrum exhibits two main contributions for the transverse optical (TO) Si–Si Raman mode: a broad Gaussian-like component located around 480 cm^{-1} and a second Lorentzian one located at 518 cm^{-1}, both related, respectively, to the amorphous and the nanocrystalline phases. The f_c values are then obtained by the following relation:[56]

$$f_c = I_c/(I_c + \gamma I_a) \tag{2}$$

with I_a and I_c the deconvoluted intensities of the Si–Si TO components located, respectively, at 480 and 518 cm^{-1}. The term γ corresponds to the ratio of the relative Raman-scattering cross sections between the amorphous and crystalline Raman modes. The γ value depends both on form and size of the crystallites. We adopt for our work a γ value of 1.423 as suggested in Ref. 56. The assumption of equivalent signal efficiency for amorphous and crystalline phases[54,57] leads to an overestimate of f_c. The crystalline Raman Si–Si TO modes of concern exhibit a high local symmetry, which removes any textural effects from the crystalline part.

Figure 11 shows the evolution of f_c with d for the films deposited on a-SiO_2. Whatever the target-substrate spacing d, f_c exceeds 60%. This is why we probably do not see any amorphous signal in the XRD diagrams, amorphous signals being broad and for such small volumes overlapped with the background, even on the nonamorphous Si substrates. Moreover, the lack of Raman shift for the Si–Si TO mode in the different analyzed films is consistent with the absence of residual stress as asserted from our XRD analyses. An abrupt increment of f_c (of around 30%) is observed for sample A

Downloaded 17 Jan 2005 to 192.93.101.134. Redistribution subject to AIP license or copyright, see http://jap.aip.org/jap/copyright.jsp

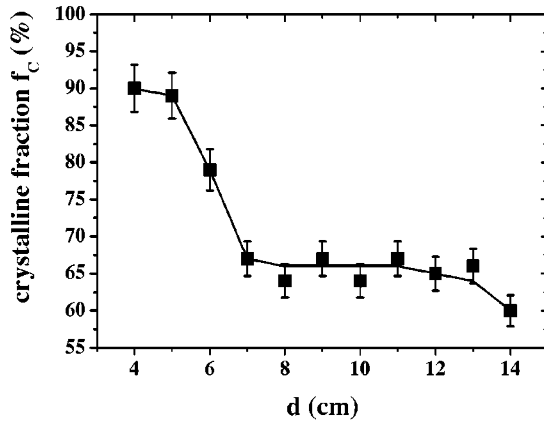

FIG. 11. Evolution of the crystalline fraction f_C vs the interelectrode distance d as deduced from Raman spectroscopy. Line is only a guide for eyes.

deposited at the closest distance (d=4 cm) in comparison with sample E (d=14 cm), that could be related to the collection of nanopowders formed in the near-cathode region for $d \leq 7$ cm, as reported elsewhere.[10]

The high f_c values (>60%) are compatible with the low concentration of bonded hydrogen C_H (lower than 1 at. %), as calculated from the integrated intensity of the FTIR band around 640 cm^{-1}.[28,58] The detection in FTIR spectra of the bending modes around 880–890 cm^{-1} suggests the presence of the SiH_2 species.[59] The decrease of the bending mode when d is lowered, is indicative of an important decrease of the SiH_2 species for $d \leq 7$ cm, region where a strong formation of Si nanopowder is observed.[10] This suggests that the formation of Si nanopowder for lower distances is due to the consumption of the highly sticking SiH_2 radicals, which become, hence, less available for the columnar growth mechanism of silicon.[60] Furthermore, we recall that the insertion of this nanopowder formed near the target is responsible for the increment of f_c considering that the Raman probes the near-surface region.[10,61] Complementary studies by mass spectrometry and optical emission spectroscopy are necessary in order to check these hypotheses via a full characterization of the reactive plasma.

D. AFM

Figure 12 shows the AFM pattern for the film deposited

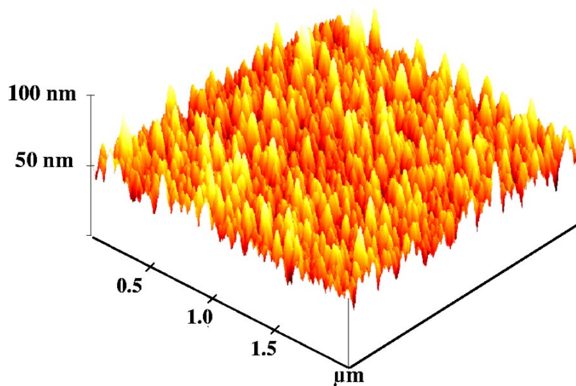

FIG. 12. Typical three-dimensional AFM micrograph for sample C (d=7 cm).

at the edge distance limiting the region of powder production (sample C, d=7 cm). Although the surface roughness has been shown to depend on the hydrogen partial pressure,[61] it remains relatively high for a degree of hydrogen-diluted argon percentage of 80% with a root-mean-square roughness r_{msq} estimated to 7 nm for this sample. This value is fully coherent with the corresponding one of 4 nm calculated from XRR curves, since porosity is located mainly at the top of the layer. Different r_{msq} values are reported in the literature: using low-pressure chemical-vapor deposition (LPCVD) and deposition temperatures around 550 °C. Modreanu *et al.*[42] obtain similar roughness (7–12 nm), while Fujiwara *et al.*[51] report values as high as 50 nm for PECVD samples deposited at temperatures comparable to ours. In this case, the PECVD seems to favor at 220 °C the growth of large crystals which induce larger roughness ranging from 18 to more than 100 nm.[29,51]

The use of radio-frequency PECVD by some authors[29,51] near 220 °C favored grain growth and then larger crystals than the ones we observed here, resulting in a considerably larger roughness, from 18 to more than 100 nm. However, the use of PECVD at 360 °C by Nakahata *et al.*[43] results in microcrystalline films exhibiting 5-nm roughness only, as determined by spectroscopic ellipsometry, for ⟨100⟩-textured samples. This would suggest some correlation between the ⟨100⟩ orientations and the low roughness, useful for thin-film transistor applications whereas rough surface could be somehow required for solar cell devices.[55] However, the use of the reactive magnetron sputtering technique allowed us to achieve lower roughness in the low deposition temperature range (200 °C), which would make the films obtained by this technique suitable for field-effect thin-film transistor devices. The low roughness observed in our films seems to be independent of the texture of the films, mono- or multicomponents, even if the ⟨100⟩ orientation would be more attractive for thin-film transistor (TFT) (due to the relatively smaller defect density induced at the oxide-silicon interface for these planes).

E. Optical properties

The detailed structural characteristics reported so far have been correlated to some physical features such as the optical properties of our layers. To this aim, optical absorption measurements have been performed and Fig. 13 compares the evolution with d of the refractive index, n, and of the Tauc *et al.*[13] gap, E_g, often used to estimate the optical band gap. The optical absorption coefficient α follows the Tauc *et al.* relation[13] in the high absorption region ($\alpha \approx 10^{-4}$ cm^{-1})

$$(\alpha E)^{1/2} = B(E - E_g), \quad (3)$$

where B is a constant and E is the incident photon energy. By plotting $(\alpha E)^{1/2}$ vs E, E_g can be obtained by the extrapolation of the linear part of the graph to the zero ordinate $[(\alpha E)^{1/2} = 0]$. The refractive index n exhibits an abrupt increase with d before some tendency to saturate for larger d values. This behavior is strictly opposite to those of the speed deposition v_d (not illustrated here) and of E_g. When v_d is low, the spe-

Downloaded 17 Jan 2005 to 192.93.101.134. Redistribution subject to AIP license or copyright, see http://jap.aip.org/jap/copyright.jsp

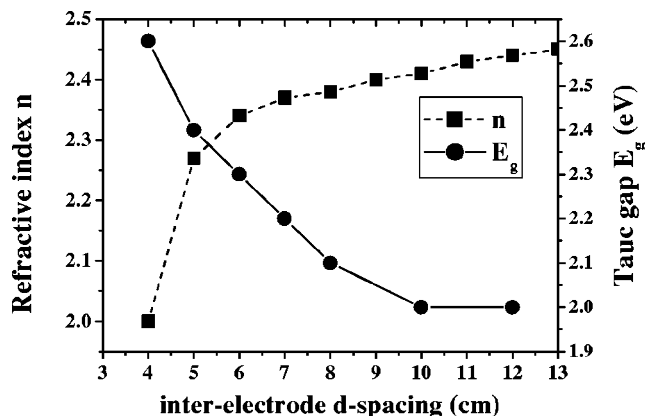

FIG. 13. Evolution of the refractive index n and of the optical gap E_g with the distance d. Lines are only guides for eyes.

cies sticking at the layer surface are more able to diffuse and contribute therefore to the relaxation of the structure. The inverse is also valid since a high v_d implies a strong rate of sticking species that hinders the diffusion at the surface and, consequently, the network relaxation. This would lead to the formation of microcavities which explains the low values of n for large d values compared to the case of close electrodes ($d < 7$ cm) where the formed nanopowders are collected, hence accentuating the porosity, as observed by our x-ray analyses. In general, our n values reflecting the presence of some microcavity density are comparable to those reported elsewhere[62,63] and would be due to the desorption of volatile species upon crystallization.[64] Concerning the Tauc *et al.* gap E_g, the relatively high values observed (Fig. 13) cannot be uniquely explained by the usual recovery of the dangling bonds by hydrogen (C_H is lower than 1 at. % in our films). Comparable values have been reported by Furukawa and Miyasato[65] that suggest an origin lying in the quantum confinement effect, which widens the gap for their 2.5-nm Si grains. As already observed by TEM, some of the Si grains in our sputtered samples, and particularly collected in the nanopowder formed for the lower d values, are smaller than the critical value for quantum confinement (5 nm), leading to widen the band gap. However, the presence of significant density of microcavities is liable to induce similarly some widening of the band gap. Consequently, it is quite reasonable to consider that the high values of E_g are due to the combined effect of the nanosized scale of some grains and to a certain porosity.

IV. CONCLUSION

A precise characterization of thin nanocrystalline silicon films prepared by reactive sputtering has been carried out using a newly developed x-ray diffraction technique as well as scattering techniques (Raman and FTIR spectroscopies), electron microscopy, and AFM measurements. In given conditions, both the target to substrate distance and the substrate nature control the crystalline fraction of the films as well as their structural, textural, and microstructural features. The grown nanocrystals exhibit anisotropic shapes elongated along the [111] direction and embedded in a partially porous and amorphous medium, and the films exhibit larger porosities near the surface. The observed textures are fiberlike but with many components varying with the distance and never reaching the exact ⟨111⟩ orientation. The film structure is free of stress and microstrain, and the unit cell of the silicon nanopowders is always larger than the bulk silicon. Slight correlation between the stabilized textures and structures could be observed, so are with the anisotropic crystal shapes. The behaviors of both the refractive index n and optical gap E_g of the films are shown to be closely correlated to these structural features, and particularly to the crystal sizes and presence of microcavities.

ACKNOWLEDGMENTS

One of the authors (Y. L.) greatly acknowledges the French Ministère de la Recherche et de la Technologie for financial support and another author (D. C.) thanks the Délégation Régionale à la Recherche et à la Technologie-région Basse-Normandie for the x-ray experimentation financing.

[1] *Proceedings of the 19th International Conference on Amorphous and Microcrystalline Semiconductors*, Nice, France, 27–31 August 2001 [J. Non-Cryst. Solids **299**, 2 (2002)].
[2] U. F. Kocks, C. N. Tomé, and H.-R. Wenk, *Texture and Anisotropy: Preferred Orientations in Polycrystals and Their Effect on Materials Properties* (Cambridge University Press, New York, 1988), Vol. 1, Chap. 6, p. 272.
[3] H. Akazawa, Phys. Rev. B **59**, 3184 (1999).
[4] P. Roca and I. Cabarrocas, J. Non-Cryst. Solids **266–269**, 31 (2000).
[5] Y. Leconte, R. Rizk, F. Gourbilleau, P. Voivenel, M. Lejeune, and C. Goncalves, Solid State Phenom. **80–81**, 65 (2001).
[6] A. Matsuda and T. Goto, Mater. Res. Soc. Symp. Proc. **164**, 3 (1990).
[7] A. Matsuda, Thin Solid Films **337**, 1 (1999).
[8] S. Veprek, M. Heintze, F. A. Sarott, M. Jurcik-Rajman, and P. Willmott, Mater. Res. Soc. Symp. Proc. **118**, 3 (1988).
[9] I. Shimizu, J. Hanna, and H. Shirai, Mater. Res. Soc. Symp. Proc. **164**, 195 (1990).
[10] Y. Leconte, P. Marie, X. Portier, M. Lejeune, and R. Rizk, Mater. Sci. Eng., B **101**, 194 (2003).
[11] G. Vignaud and A. Gibaud, computer code REFLEX (http://lpec.univ-lemans.fr/reflex/reflex.htm, 2000).
[12] B. Garrido, A. Perez-Rodriguez, J. R. Morante, A. Achik, P. Gourbilleau, R. Madelon, and R. Rizk, J. Vac. Sci. Technol. B **16**, 1851 (1998).
[13] J. Tauc, R. Grigorovici, and A. Vancu, Phys. Status Solidi **15**, 627 (1966).
[14] J. Ricote and D. Chateigner, Bol. Soc. Esp. Ceram. Vidrio **38**, 587 (1999).
[15] L. Lutterotti, H.-R. Wenk, and S. Matthies, in *Textures of Materials*, edited by J. A. Szpunar (NRC Research, Ottawa, 1999), Vol. 2, pp. 1599–1604.
[16] S. Matthies and G. W. Vinel, Phys. Status Solidi B **112**, K111 (1982).
[17] J. J. Heizmann and C. Laruelle, J. Appl. Crystallogr. **19**, 467 (1986).
[18] http://pcb4122.univ-lemans.fr/powdif/low_fwhm_and_rp.html#t4B
[19] D. Balzar, J. Appl. Crystallogr. **25**, 559 (1992).
[20] N. C. Popa, J. Appl. Crystallogr. **31**, 176 (1998).
[21] M. Morales, D. Chateigner, L. Lutterotti, and J. Ricote, Mater. Sci. Forum **408–412**, 113 (2002).
[22] S. Matthies, G. W. Vinel, and K. Helming, *Standard Distributions in Texture Analysis* (Akademie, Berlin, 1987), Vol. 1, p. 449.
[23] H.-J. Bunge, *Texture Analysis in Material Science* (Butterworths, London, 1982).
[24] GOMAN, INEL France SA Licence 1997; POFINT: "Pole figure interpretation," CNRS-INEL France SA Licence 2002.
[25] H.-R. Wenk, S. Matthies, J. Donavan, and D. Chateigner, J. Appl. Crystallogr. **31**, 262 (1998).
[26] A. Guinier, *Théorie et Techniques de la Radiocristallographie*, 3rd ed. (Dunod, Paris, 1964).
[27] J. I. Lanford and D. Louer, J. Appl. Crystallogr. **15**, 20 (1982).
[28] Y. Feng, M. Zhu, F. Liu, J. Liu, H. Han, and Y. Han, Thin Solid Films **395**, 213 (2001).
[29] E. Vallat-Sauvain, U. Kroll, J. Meier, and A. Shah, J. Appl. Phys. **87**, 3137 (2000).
[30] U. Kroll, J. Meir, P. Torres, J. Pohl, and A. Shah, J. Non-Cryst. Solids

Downloaded 17 Jan 2005 to 192.93.101.134. Redistribution subject to AIP license or copyright, see http://jap.aip.org/jap/copyright.jsp

227–230, 69 (1998).
[31]D. Balzar and S. Popovic, J. Appl. Crystallogr. **29**, 16-23 (1996).
[32]L. Houben, M. Luysberg, and R. Carius, Phys. Rev. B **67**, 045312 (2003).
[33]L. Lutterotti, S. Matthies, H.-R. Wenk, A. S. Schultz, and J. W. Richardson Jr., J. Appl. Phys. **81**, 594 (1997).
[34]D. Chateigner, in *Combined Analysis: Structure-Texture-Microstructure-Phase-Stresses Determination by X-ray and Neutron Diffraction* (2004); http://www.ensicaen.ismra.fr/~chateign/texture/combined.pdf
[35]K. Helming, Textures Microstruct. **14–18**, 187 (1991).
[36]R. J. Hill and R. X. Fisher, J. Appl. Phys. **23**, 462 (1990).
[37]W. A. Dollase, J. Appl. Crystallogr. **19**, 267 (1986).
[38]F. K. Lotgering, J. Inorg. Nucl. Chem. **9**, 113 (1959).
[39]T. Kamiya, K. Nakahata, K. Ro, C. M. Fortmann, and I. Shimizu, Jpn. J. Appl. Phys., Part 1 **38**, 5750 (1999).
[40]C. Faivre and D. Bellet, J. Appl. Crystallogr. **32**, 1134 (1999).
[41]D. Chateigner, F. Brunet, A. Deneuville, P. Germi, M. Pernet, and P. Gonon, J. Cryst. Growth **148**, 110 (1995).
[42]M. Modreanu, N. Tomozeiu, M. Gartner, and P. Cosmin, Thin Solid Films **383**, 254 (2001).
[43]K. Nakahata, A. Miida, T. Kamiya, Y. Maeda, C. M. Fortmann, and I. Shimizu, Jpn. J. Appl. Phys., Part 2 **37**, L1026 (1998).
[44]S.-I. Ishibara, D. He, M. Nakata, and I. Shimizu, Jpn. J. Appl. Phys., Part 1 **32**, 1539 (1993).
[45]T. I. Kamins and T. R. Cass, Thin Solid Films **16**, 147 (1973).
[46]T. I. Kamins, Sens. Actuators, A **21–23**, 817 (1990).
[47]J. Yang, K. Kahn, A.-Q. He, S. M. Phillips, and A. H. Heuer, J. Microelectromech. Syst. **9**, 485 (2000).
[48]M. Birkholz, B. Selle, E. Conrad, K. Lips, and W. Fuhs, J. Appl. Phys. **88**, 4376 (2000).
[49]R. Bisaro, J. Maraino, N. Proust, and K. Zellama, J. Appl. Phys. **59**, 1167 (1986).
[50]T. I. Kamins, *Polycrystalline Silicon for Integrated Circuit Applications* (Kluwer, Boston, 1988).
[51]H. Fujiwara, M. Kondo, and A. Matsuda, Phys. Rev. B **63**, 115306 (2001).
[52]J. Daillant, *X-ray and Neutron Reflectivity: Principles and Applications* (Springer, Berlin, 1999), p. 95.
[53]D. Buttard, G. Dolino, D. Bellet, T. Baumbach, and F. Rieutord, Solid State Commun. **109**, 1 (1999).
[54]S.-I. Ishibara, D. He, and I. Shimizu, Jpn. J. Appl. Phys., Part 1 **33**, 51 (1994).
[55]T. Unagami, A. Lousa, and R. Messier, Jpn. J. Appl. Phys., Part 2 **36**, L737 (1997).
[56]E. Bustaret, M. A. Hachicha, and M. Brunel, Appl. Phys. Lett. **52**, 1675 (1988).
[57]F. Liu, M. Zhu, J. Liu, and L. Wang, Thin Solid Films **430**, 182 (2003).
[58]A. Achiq, R. Rizk, F. Gourbilleau, and P. Voivenel, Thin Solid Films **348**, 74 (1999).
[59]G. Lucovsky, R. J. Nemanich, and J. G. Knights, Phys. Rev. B **19**, 2074 (1979).
[60]Y. Leconte, P. Marie, X. Portier, M. Lejeune, and R. Rizk, Thin Solid Films **427**, 252 (2003).
[61]Y. Leconte, C. Dufour, B. Garrido, and R. Rizk, J. Non-Cryst. Solids **299–302**, 87 (2002).
[62]G. N. Parsons, J. J. Bolland, and J. C. Tsang, Jpn. J. Appl. Phys., Part 1 **31**, 1943 (1992).
[63]I. Shimizu, J. Non-Cryst. Solids **114**, 145 (1989).
[64]T. Akasaka and I. Shimizu, Appl. Phys. Lett. **66**, 3441 (1995).
[65]S. Furukawa and T. Miyasato, Phys. Rev. B **38**, 5726 (1988).

Downloaded 17 Jan 2005 to 192.93.101.134. Redistribution subject to AIP license or copyright, see http://jap.aip.org/jap/copyright.jsp